Heliyon 10 (2024) e37271

Contents lists available at ScienceDirect

Heliyon

journal homepage: www.cell.com/heliyon

Research article

# A numerical analysis of metal-supported solid oxide fuel cell with a focus on temperature field

Mengru Zhang [a], Enhua Wang [a,*], Meng Ni [b,**], Keqing Zheng [c], Minggao Ouyang [d], Haoran Hu [d,e], Hewu Wang [d], Languang Lu [d], Dongsheng Ren [d], Youpeng Chen [e]

[a] School of Mechanical Engineering, Beijing Institute of Technology, Beijing, 100081, China
[b] Department of Building and Real Estate, Research Institute for Sustainable Urban Development (RISUD) & Research Institute for Smart Energy (RISE), The Hong Kong Polytechnic University, Hung Hom, Kowloon, Hong Kong, China
[c] School of Electrical and Power Engineering, China University of Mining and Technology, Xuzhou, 221166, China
[d] State Key Laboratory of Automotive Safety and Energy, Tsinghua University, Beijing, 100084, China
[e] Beijing Swift New Energy Technologies Co., Ltd., Beijing, 100192, China

ARTICLE INFO

*Keywords:*
Metal-supported solid oxide fuel cell
Ceria-based multi-layer electrolyte
Multi-physical model
Radiation
Comprehensive field analysis

ABSTRACT

Metal-supported solid oxide fuel cell (MS-SOFC) is very promising for intermediate temperature solid oxide fuel cell (SOFC) due to better mechanical strength, low materials cost, and simplified stack assembling. However, the effects of metal support on the performance and temperature field of MS-SOFC is still necessary for further study. In this study, a three-dimensional multi-physical model is developed to investigate how the use of metal support influence the electrochemical performance and the temperature field of MS-SOFC with a ceria-based electrolyte. The multi-physical model fully considers the conservation equations of mass, momentum, and energy that are coupled with mass transport and electrochemical reactions. The wall temperature in the radiation model is calculated using a discrete method. It is found that the radiation heat flux accounts for 3.13 % of the total heat flux. More importantly, the temperature difference of MS-SOFC is 3.61 % lower than that of conventional anode-supported SOFC, leading to improved temperature uniformity and cell durability.

## 1. Introduction

SOFC is a high-efficiency clean power generation device [1–3]. Early SOFCs are based on tubular configurations, which have high mechanical strength and easy for sealing but suffer from high ohmic loss due to the long electron conduction path along the perimeter of the tubes [4]. For comparison, planar SOFC features easy stacking, promising fabrication of large cells, and low ohmic loss due to short path for electron conduction [5,6]. For planar SOFCs, one layer needs to be sufficiently thick to provide the required mechanical strength [7]. The electrolyte-supported SOFC (ES-SOFC) with a thick electrolyte layer suffers from significant ohmic loss which is proportional to the thickness of the electrolyte [8,9]. While cathode-supported SOFC (CS-SOFC) with a thick cathode layer suffers from serious cathode concentration loss due to the slow diffusion of $O_2$ through the porous cathode. For comparison, the diffusion of $H_2$ is

* Corresponding author.
** Corresponding author.
*E-mail addresses:* wangenhua@bit.edu.cn (E. Wang), meng.ni@polyu.edu.hk (M. Ni).

https://doi.org/10.1016/j.heliyon.2024.e37271
Received 15 August 2024; Received in revised form 27 August 2024; Accepted 29 August 2024
Available online 4 September 2024

fast and would not cause high concentration loss even with a thick anode layer [10]. Thus, the anode-supported configuration is popular for planar SOFCs. However, the anode-supported SOFC with porous anode support may experience crystal phase change of Ni-YSZ (typical composite anode material) in the long-term operation, which could cause volume change of the anode, leading to poor contact between the anode and the electrolyte and poor durability [11].

To achieve optimal design of planar SOFC, a thorough consideration of mass and heat transfer, and electrochemical reactions is necessary to obtain distributions of current density, power density, and concentrations of reactants and products. On this basis, a preliminary simulation model can be used to optimize the fuel cell (FC)at a lower cost compared to direct experiments based on trial and error [12,13]. This makes computational fluid dynamics (CFD) an essential tool in the iterative design process [14–16]. Shen et al. [17] developed a two-dimensional CFD model and investigated the heat and mass transfer characteristics in an anode-supported SOFC (AS-SOFC) under diverse operational conditions. The overall cell performance and local temperature distribution were analyzed considering the effects of operating temperature, flow direction arrangement, and flow velocity. The results showed that increasing the operating temperature and reducing the cathode flow velocity resulted in an increase in local temperature. Moreover, a significant change in the temperature distribution occurred when the counter-flow arrangement was used instead of co-flow arrangement. Additionally, it was found that the effect of anode flow velocity on temperature distribution was negligible. Russner et al. [18] built a 2D model and finite element method was employed to estimate the underlying chemical and physical processes. Both the electrical performance and temperature distributions of planar SOFC stack layers were determined when operating with reformate fuels. The numerical study revealed the different performances of AS-SOFC and ES-SOFC, demonstrating how operational conditions affected the electrical performance and temperature distribution, and elucidating how individual loss contributions influenced the temperature distributions within the stack layer. Zeng et al. [19] established a 3D simulation model that considered radiation heat transfer and discovered that radiation could significantly affect the performance of SOFC. The maximum temperatures inside the SOFC were 1124.19 K and 1109.79 K when the emissivity was 0 and 1, respectively. Tan et al. [20] built a quasi-3D numerical model of an SOFC short stack and investigated the impact of flow configurations. The counter-flow stack achieved the highest voltage efficiency among the co-, counter-, and cross-flow configurations, and exhibited significant dispersion in current density distribution on the cells. Chen et al. [21] developed a 3D electrochemical multi-physical model to investigate the impact of the new parallel-cylindrical flow field on SOFC performance. The new parallel-cylindrical flow field increased the current density by 38 % and improved the reactant distribution uniformity by 60 %. Liu et al. [22] developed a 3D model coupling mass transfer, charge transport, and electrochemical reactions based on CFD. The impact of novel parallel S-type flow channels on ammonia decomposition and the electrical performance of direct ammonia solid oxide fuel cell (DA-SOFC) were investigated, and four channel arrangements were compared including conventional unbent channels, single type channels, double S-type channels, and triple S-type channels. The results showed that S-type channels exhibited self-heating effect due to heat released from electrochemical reactions in the rear supporting ammonia decomposition in the front part of the channel, enhancing $H_2$ concentration and electrochemical reaction rates. Guo et al. [23] utilized three-dimension CFD to compare the operating performances of various interconnector (IC) designs, including discrete rectangular solid ribs, discrete cylindrical ribs, discrete rhombus ribs, narrowed ribs and channels, wave-like ribs, trapezoid ribs, staggered cuboid ribs, and parallel traditional IC. The results indicated that the new IC design achieved a more uniform distribution of $O_2$ in the cathode, resulting in a 27.86 % increase in peak power density of the SOFC compared to the conventional parallel IC. Iibas et al. [24] studied the effects of parameters on a CS-SOFC and an ES-SOFC based on multi-physical models. Compared to the ES-SOFC, the CS-SOFC showed a higher performance.

Compared with conventional planar SOFCs, MS-SOFC appeared in recent years as a promising design due to the high mechanical strength and low cost. MS-SOFC has demonstrated excellent reliability and durability by operating at low to medium temperatures below 700 °C [25–28]. However, current research on MS-SOFC mainly relied on zero-dimensional models, without considering the distribution of the physical quantities in the MS-SOFC [28,29]. Only Park et al. established 3D model of MS-SOFC with an operating temperature of 750–850 °C, but did not consider the influence of radiation on temperature field [30]. Some researchers have found that the radiation heat transfer had a significant effect on the heat transfer rate [31]. More importantly, the use of metal support with a high thermal conductivity may facilitate the heat transfer process, which in turn could influence the thermal stress and the electrochemical performance of the MS-SOFC. However, no study has been conducted to systematically investigate how the use of metal support influences the temperature field and the electrochemical performance of MS-SOFC. To fill in this research gap, a 3D multi-physical model is developed to numerically study the MS-SOFC. Considering the lower operation temperature of about 650 °C, ceria-based electrolyte is used. Unlike the existing models on MS-SOFC in the literature, the model reported in this study fully considers the coupled transport and electrochemical reaction processes, in particular, the radiative heat transfer process is considered.

## 2. Methodology

Ceria-based electrolytes, such as gadolinium-doped ceria (GDC) and Samaria-doped ceria (SDC), exhibit a higher ionic conductivity at temperatures ranging from 500 to 700 °C compared to conventional yttrium-stabilized zirconia (YSZ). Currently, GDC is employed in the MS-SOFC developed by Ceres Power Ltd. Nevertheless, GDC suffers from significant electronic leakage at high temperatures. Ceres Power Ltd. [32] designed an MS-SOFC with a triple-layer electrolyte to inhibit electronic leakage, which was studied by Zhang et al. [29] as well. In this study, an MS-SOFC with the same structure is employed. A triple-layer electrolyte structure of $Ce_{0.9}Gd_{0.1}O_{2-\delta}|(Y_2O_3)_{0.04}(ZrO_2)_{0.92}|Ce_{0.9}Gd_{0.1}O_{2-\delta}$ (GDC|YSZ|GDC), in which YSZ is used to inhibit electron conduction through the electrolyte layer. GDC is used as the main electrolyte with a thickness of 10 μm. A layer of YSZ in 1 μm is deposited on the surface of GDC as a barrier layer to prevent electronic leakage. In addition, a 0.2 μm GDC thin layer is deposited on the YSZ layer as a barrier layer to avoid the direct solid reaction between YSZ and the cathode material $La_{0.6}Sr_{0.4}Co_{0.2}Fe_{0.8}O_{3-\delta}$ (LSCF) and the formation of a low-conductivity

impure phase. The anode (Ni/GDC) and cathode (LSCF/GDC) are the same as that of the MS-SOFC of Ceres Power Co., Ltd. A porous metal support layer is used beneath the anode to provide enough mechanical strength to the entire cell. The working principle of MS-SOFC is illustrated as follows. In operation, the fuel (normally hydrogen) and the air are supplied to the anode and the cathode, respectively. Oxygen is reduced at the cathode, producing oxygen ions, which are conducted to the anode layer through the dense electrolyte. At the anode side, the oxygen ions react with hydrogen to generate water and electrons. The water is taken away via the anode channel while the electrons are transported to the cathode through the external circuit to produce useful power. A 3D model for the single channel of the cell is established for the MS-SOFC, as shown in Fig. 1. The model consists of the interconnect with parallel flow channels, the anode flow channel, the metal support layer, the anode reaction layer, the triple-layer electrolyte GDC|YSZ|GDC, the cathode reaction layer, the cathode diffusion layer, and the cathode flow channel. Table 1 lists the specific geometric parameters of the MS-SOFC.

According to the established geometric and multi-physical model, the following assumptions are specified for the 3D numerical simulation.

(1) The channel shape is rectangular;
(2) All gases are ideal;
(3) The pressures at the outlets of the anode and cathode are 0.1 MPa;
(4) The temperature of the fluid at the inlet of the anode or the cathode is constant;
(5) The flow inside the flow passages is laminar.

### 2.1. Governing equations

The electrochemical reactions occurring in the anode and cathode of the MS-SOFC can be expressed by [33,34]:

$$H_2 + O^{2-} \rightarrow H_2O + 2e^- \tag{1}$$

$$\frac{1}{2}O_2 + 2e^- \rightarrow O^{2-} \tag{2}$$

The multi-physical model fully considers fluid flow, mass transport, and electrochemical reactions. For gas flow in the channel, a laminar flow is assumed due to the low Reynolds number. The governing equations for fluid flow include the continuity, momentum, and energy equations. The Navier-Stokes equation for incompressible flow is used to describe the flows in the anode and cathode channels [21,23].

$$(\rho \boldsymbol{u}\nabla)\cdot \mathbf{u} = -\nabla p + \nabla \cdot \left\{ \mu\left[\nabla \boldsymbol{u} + (\nabla \boldsymbol{u})^T\right] - \frac{2}{3}\mu(\nabla \boldsymbol{u}) \right\} \tag{3}$$

The Brinkman equation is employed to describe the flow in the porous electrodes.

$$\frac{\rho}{\varepsilon}(\boldsymbol{u}\cdot\nabla)\cdot\frac{\boldsymbol{u}}{\varepsilon} = -\nabla p + \nabla \cdot \left\{ \frac{\mu}{\varepsilon}\left[\nabla \boldsymbol{u} + (\nabla \boldsymbol{u})^T\right] - \frac{2}{3}\frac{\mu}{\varepsilon}(\nabla \cdot \boldsymbol{u}) \right\} - \left(\mu k^{-1} + \frac{S_m}{\varepsilon^2}\right)\boldsymbol{u} \tag{4}$$

where $\mu$ is the dynamic viscosity of the gas mixture, $\boldsymbol{u}$ is the velocity vector ($m\cdot s^{-1}$), $\rho$ is the density ($kg\cdot m^{-3}$), $T$ is the temperature (K), $\kappa$ is the permeability of the porous media ($m^2$), $\varepsilon$ is the porosity of the porous media, and $S_m$ is the source term of continuity, which can be expressed:

$$S_m^{an} = S_{H_2} + S_{H_2O} \tag{5}$$

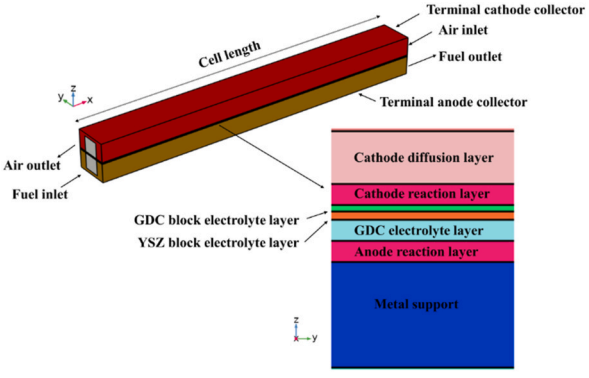


**Fig. 1.** Geometric model of the single-channel MS-SOFC.

**Table 1**
Geometric parameters of the designed MS-SOFC.

| Geometry | Value | Unit |
|---|---|---|
| Flow channel length | $8.0 \times 10^{-2}$ | m |
| Flow channel height | $1.0 \times 10^{-3}$ | m |
| Flow channel width | $1.0 \times 10^{-3}$ | m |
| Anode reaction layer thickness | $10.0 \times 10^{-6}$ | m |
| GDC main electrolyte thickness | $10.0 \times 10^{-6}$ | m |
| YSZ thickness | $1.0 \times 10^{-6}$ | m |
| GDC barrier layer thickness | $0.2 \times 10^{-6}$ | m |
| Cathode reaction layer thickness | $10.0 \times 10^{-6}$ | m |
| Cathode diffusion layer thickness | $25.0 \times 10^{-6}$ | m |
| Metal support thickness | $100.0 \times 10^{-6}$ | m |
| Interconnector height | $1.2 \times 10^{-3}$ | m |
| Interconnector width | $2.0 \times 10^{-3}$ | m |

$$S_m^{ca} = S_{O_2} \tag{6}$$

The mass transfer due to diffusion is modeled by the Maxwell-Stefan equation involving the Knudsen diffusion [35].

$$\nabla\left( -\rho\omega_i \sum D_{ij}^{eff}\left(\nabla x_i + (x_i - \omega_i)\frac{\nabla p}{p}\right) + \rho\omega_i \boldsymbol{u}\right) = S_i \tag{7}$$

where $\omega_i$ is mass fraction of species $i$, $x_i$ is the molar fraction of species $i$, $p$ is the pressure (Pa), and $D_{ij}^{eff}$ is the effective diffusion coefficient ($m^2$·s) [36,37].

$$D_{ij}^{eff} = \frac{\varepsilon}{\tau}\left(\frac{1}{D_{ij}} + \frac{1}{D_{ik}}\right)^{-1} \tag{8}$$

where $D_{ij}$ is the binary diffusion coefficient and $D_{ik}$ is the Knudsen coefficient for the specie $i$ ($m^2$·s). The source term $S_i$ is the production or consumption of species $i$ owing to the electrochemical reactions, which are expressed as follows:

$$S_{H_2} = -\frac{j}{2F} Mw_{H_2} \tag{9}$$

$$S_{H_2O} = -\frac{j}{2F} Mw_{H_2O} \tag{10}$$

$$S_O = -\frac{j}{4F} Mw_{O_2} \tag{11}$$

where F is the Faraday constant (C·$mol^{-1}$), $j$ is the current density (A·$m^{-2}$), $Mw_i$ is the molecular weight of species (kg·$mol^{-1}$).

The conservation equation of electronic charge transport for the electrode and electrolyte is denoted by

$$\nabla \cdot ( -\sigma_{el} \nabla \varphi_{el}) = S_{el} \tag{12}$$

The conservation of ionic charge transfer is represented by

$$\nabla \cdot ( -\sigma_{io} \nabla \varphi_{io}) = -S_{io} \tag{13}$$

where $\sigma_{el}$ and $\sigma_{io}$ are the electronic conductivity and ionic conductivity (S·$m^{-1}$), respectively. $\varphi_{el}$ and $\varphi_{io}$ are the electronic and ionic potentials (V), respectively.

The Butler-Volmer equation is employed to model the activation overpotential and the effects of the concentrations are also considered [38,39].

For the anode,

$$i_a = A_v i_{0,ref}^{H_2}\left(\frac{C_{H_2}}{C_{H_2,ref}}\right)^{\gamma_{H_2}}\left[\exp\left(\frac{\alpha n F \eta_{act,a}}{RT}\right) - \exp\left(\frac{(1-\alpha) n F \eta_{act,a}}{RT}\right)\right] \tag{14}$$

For the cathode,

$$i_c = A_v i_{0,ref}^{O_2}\left(\frac{C_{O_2}}{C_{O_2,ref}}\right)^{\gamma_{O_2}}\left[\exp\left(\frac{\alpha n F \eta_{act,c}}{RT}\right) - \exp\left(\frac{(1-\alpha) n F \eta_{act,c}}{RT}\right)\right] \tag{15}$$

where $i_{0,ref}^{H_2}$ and $i_{0,ref}^{O_2}$ are the reference exchange current densities for $H_2$ oxidation and $O_2$ reduction reactions (A·$m^{-2}$) at the reference

concentrations, $C_{H_{2,ref}}$ and $C_{O_{2,ref}}$, respectively, R is the ideal gas constant (J·mol$^{-1}$·K$^{-1}$), and $\eta$ is the activation overpotential (V), a is the charge transfer coefficient (or symmetry factor), whose value is 0.5. The reactive surface area per unit volume ($A_v$) is determined based on the random packing of binary spherical particles proposed by Costamagna et al. [40–42].

With regard to the energy equation, the local thermal equilibrium assumption is used in the heat transfer model [43,44].

$$\nabla \cdot (-\lambda \cdot \nabla T) = S_q - \rho C_p \boldsymbol{u} \cdot \nabla T \tag{16}$$

where $\lambda$ is the volumetric average thermal conductivity (W·m$^{-1}$·K$^{-1}$), $C_p$ is the specific heat capacity (J·kg$^{-1}$·K$^{-1}$). $S_q$ is the source term computed in Eqs. 18–20.

The volumetric average thermal conductivity $\lambda$ consists of two parts, the solid and the fluid, and is determined by

$$\lambda = \varepsilon\lambda_f + (1-\varepsilon)\lambda_s \tag{17}$$

where ε is porosity of solid, the subscripts $f$ and $s$ refer to the fluid and the solid, respectively.

Only electronic conductivity exists in the interconnect and the metal support as well as the diffusion layer of the cathode. Hence,

$$S_{q\_e} = \sigma_{el}\nabla\varphi_{el} \cdot \nabla\varphi_{el} \tag{18}$$

In the electrolyte, the conductivity of the oxygen ions is modeled by

$$S_{q\_i} = \sigma_{io}\nabla\varphi_{io} \cdot \nabla\varphi_{io} \tag{19}$$

Both the electronic and ionic conductivities are considered in the reaction layers of the anode and the cathode.

$$S_q = \sigma_{el}\nabla\varphi_{el} \cdot \nabla\varphi_{el} + \sigma_{io}\nabla\varphi_{io} \cdot \nabla\varphi_{io} - \frac{J}{2F}T\Delta S - J\eta_{act} \tag{20}$$

The heat flux including net radiative heat flux for the air and fuel channels determined by

$$n \cdot (-\lambda\nabla T) = q_r \tag{21}$$

where $q_r$ is the net heat radiative transfer rate from the electrode surface to the interconnect surface (W·m$^{-2}$).

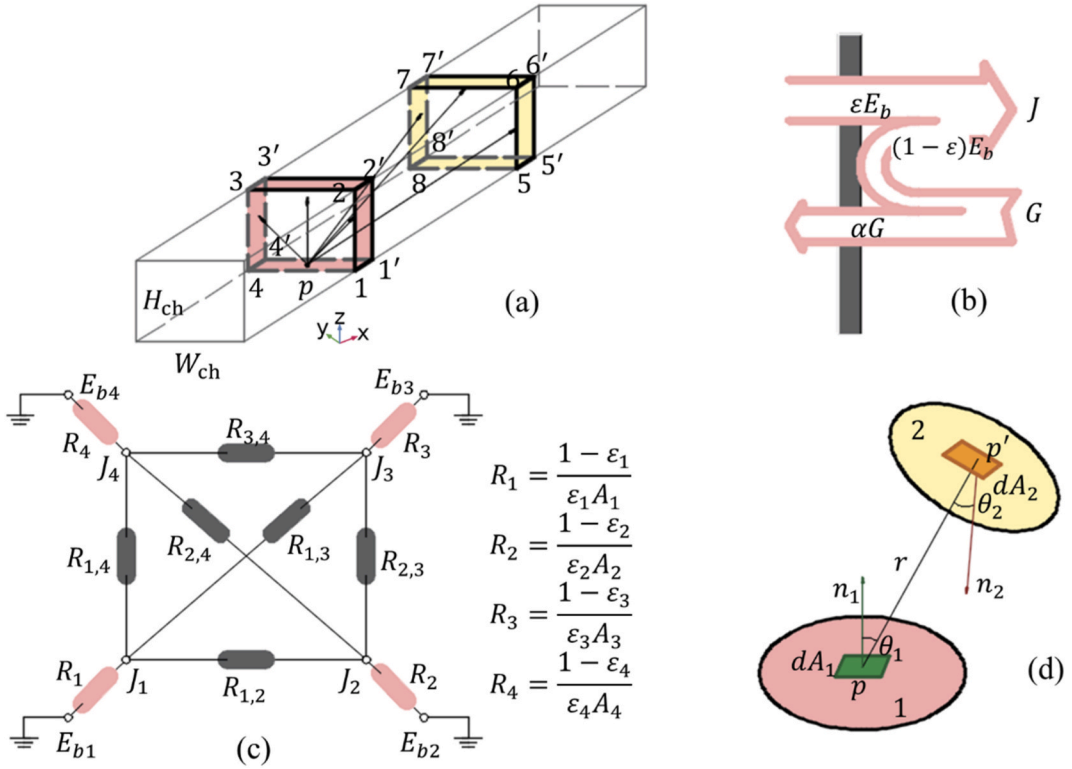


**Fig. 2.** Radiation in MS-SOFC: (a) the configuration for diffuse interchange in the MS-SOFC; (b) radiation heat transfer between gray surfaces; (c) thermal radiation equivalent network diagram for surface to interconnect in the MS-SOFC; (d) radiation heat transfer between two faces at arbitrary.

### 2.2. Thermal radiation model

The temperature is particularly important for the durability of SOFC. Therefore, an accurate temperature field model is needed to estimate the internal temperature distribution. At present, the literature on SOFC have found that the surface radiation heat transfer between electrodes and interconnects accounted for a significant proportion in SOFC [19,45]. However, such a description of radiation is only available for traditional SOFC under a temperature above 800 °C. For MS-SOFC operating at medium and low temperatures, there is still no report regarding radiation; in addition, previous investigation calculated the amount of surface radiation heat transfer between the electrode and the interconnect, assuming that the temperature of the interconnect was equal to the furnace temperature [19]. In this paper, the MS-SOFC is divided into ten separate parts and the local temperature of each part is solved separately considering radiation heat transfer. Each individual's electrode surface exchanges heat with the connecting body surfaces of all individuals through radiation, two selected in particular for display, as shown in Fig. 2(a).

The integral equation of radiation is rather complex, typically depending on multiple independent variables such as time, spatial variables, angular variables describing the direction of radiation propagation and wavelength. In addition, due to the fourth power dependence of emission power on temperature, the control equation is non-linear. Apart from the difficulties associated with solving these equations, the accuracy of any analysis is always subject to the nature of the known radiation characteristics. Therefore, for the purpose of conducting a simple radiation analysis, this study assumes that all surfaces inside the channel are opaque, diffuse, and gray. The method of determining the surface net radiation heat transfer rate based on radiation quantity includes concepts such as radiosity and irradiation, as shown in Fig. 2(b), (c), and (d).

Fig. 2(b) shows the radiosity, which indicates the rate at which radiation leaves a unit area of a surface in all directions [46]. As shown in Fig. 2(c),the Kirchhoff's law of radiation is used to calculate the radiation between diffuse gray surfaces. For an opaque surface, the radiosity can be presented as:

$$\mathrm{J} = (1-\varepsilon)\mathrm{G} + \varepsilon\sigma T^4 \tag{22}$$

where J is the radiosity ($\mathrm{W{\cdot}m^{-2}}$); ε is the surface emissivity; G is the irradiation ($\mathrm{W{\cdot}m^{-2}}$); σ is the Stefan-Boltzmann constant, $5.67 \times 10^{-8}$ $\mathrm{W\ m^{-2}\ K^{-4}}$.

The radiation flux incident on a surface from all directions is called irradiation G, and is expressed as:

$$\mathrm{G} = G_p + F_{amb}\sigma T_{amb}^4 \tag{23}$$

where $G_p$ is the mutual irradiation ($\mathrm{W{\cdot}m^{-2}}$), being from other surfaces in the model; $F_{amb}$ is the ambient view factor [47]; $T_{amb}$ is the ambient temperature (K).

As shown in Fig. 2(d), for the specific point, $\boldsymbol{p}(x,y,z)$, in a surface, the irradiation of the point $\boldsymbol{p}'(x', y', z')$ to the point $\boldsymbol{p}(x,y,z)$ can be defined as:

$$G_p = \int_0^{A'} \frac{(-\boldsymbol{n}'\cdot\boldsymbol{r})(\boldsymbol{n}\cdot\boldsymbol{r})}{\pi|\boldsymbol{r}|^4} J' dA \tag{24}$$

where A is the wall surface area ($\mathrm{m^2}$); $n'$ is the unit normal factor of $\boldsymbol{p}'(x', y', z')$ in solid surface; $\boldsymbol{r}$ is the vector from the point $\boldsymbol{p}(x,y,z)$ to $\boldsymbol{p}'(x', y', z')$; $\boldsymbol{n}$ is the unit normal factor of $\boldsymbol{p}(x,y,z)$ in solid surface; $J'$ is the radiosity of $\boldsymbol{p}'(x', y', z')$.

The ambient view factor is evaluated by

$$F_{amb} = 1 - \left(X_{1,2} + X_{1,3} + \ldots + X_{1,n}\right) \tag{25}$$

where $X_{1,n}$ is the configuration factor and given by

$$X_{1,n} = \int_0^{A_n'} \frac{(-\boldsymbol{n}'\cdot\boldsymbol{r})(\boldsymbol{n}\cdot\boldsymbol{r})}{\pi|\boldsymbol{r}|^4} dA_n \tag{26}$$

According to the energy balance, the net flux of the heat transfer from a surface is denoted by $q_r$ and is expressed as

$$q_r = \mathrm{J} - \mathrm{G} \tag{27}$$

With Eqs. (22), (23) and (27), the net radiation heat transfer rate can be received.

**Table 2**
Thermophysical properties of materials of the MS-SOFC.

| Property | Density ($\mathrm{kg{\cdot}m^{-3}}$) | Specific heat ($\mathrm{J{\cdot}kg^{-1}{\cdot}K^{-1}}$) | Thermal conductivity ($\mathrm{W{\cdot}m^{-1}{\cdot}K^{-1}}$) | Ref. |
|---|---|---|---|---|
| Anode | 6870 | 595 | 6 | [19,49] |
| Electrolyte | 5900 | 606 | 2.7 | [19,49] |
| Cathode | 3310 | 430 | 11 | [19,50] |
| Interconnector/metal support | 3030 | 550 | 20 | [19,23] |

### 2.3. Boundary conditions

The thermal and physical properties of the materials in the MS-SOFC are given in Table 2. The main parameters of the cell are listed in Table 3 and other parameters can be referenced in Refs. [19,48]. The gas flow of the MS-SOFC is counter-flow configuration.

The boundary conditions for the multi-physical model are listed in Table 4.

### 2.4. Model validation

The 3D model is built in COMSOL. Fig. 3(a) shows the results of the mesh independence test. The operating voltage is set to 0.75 V and the emissivity is 0.80. The cell length is set to 8 cm. The gas flow of the MS-SOFC is counter-flow configuration. A tetrahedral mesh is employed. The variation of the average temperatures at the outlets of the fuel and the air sides are plotted for five different mesh numbers 8,400, 10,920, 15,960, 24,360, and 42,000. When the mesh number is greater than 24,360, the average temperatures tend to be converged. Considering the computational load, the mesh with a cell number of 24,360 is selected for the following 3D simulation. On the other hand, the precision of the established CFD model is compared with those in literature. Specifically, to be consistent with Ref. [19], the cell length of Fig. 3(b) and (c) are set to 2 cm. Subsequently, the radiation heat transfer model of AS-SOFC is validated and the results are shown in Fig. 3(b). The simulated profile is in good consistency with the data and the deviations are within 3.05 %. Additionally, Fig. 3(c) shows a comparison of the temperature distribution between the MS-SOFC and the AS-SOFC in Ref. [19] using the same operation conditions with a co-current flow arrangement. It can be seen that the tendencies of temperature distribution are not exactly the same because the electrolyte GDC is used in the MS-SOFC instead of YSZ in the AS-SOFC. The upper part of the reference AS-SOFC model is the anode side and the lower part is the cathode side. The layout of the MS-SOFC is similar. The emissivity is set to 1. At the position X = 0.2 cm, the highest temperature occurs near the electrolyte and the lowest temperature occurs in the cathodic flow channel. The minimum and maximum temperatures of the reference model are 1083.2 K and 1084.3 K, respectively. The minimum and maximum temperatures of the MS-SOFC model in this study are 1074.73 K and 1078.68 K, respectively, with an error of 0.78 % and 0.49 %. Therefore, the established CFD model manifests an acceptable accuracy. Fig. 3(d) shows a comparison of the polarization curve of the MS-SOFC with the experimental data from Ceres Power Ltd [28]. when the operating temperature is 600 °C. The cell length is set to 8 cm. The variation trends are consistent, and the average relative deviation is 17.28 %.

## 3. Results and discussion

The 3D simulation is performed at 923.15 K and 0.1 MPa. The fuel mixture (97 % hydrogen and 3 % steam) is supplied to the anode from the left in a speed of 0.89 m $s^{-1}$ and the air is delivered to the cathode from the right in a speed of 3.44 m $s^{-1}$. The results are obtained and the effects of radiation on the temperature fields and the performance of the MS-SOFC are analyzed in detail.

### 3.1. Influence of radiation on the temperature field of MS-SOFC

In the heat transfer model of SOFC, the phenomenon of radiation is often ignored. However, SOFCs operate at high temperatures and radiation is inevitable. Hence, the accuracy of the model is affected. The heat transfer caused by radiation is relatively significant, which is proportional to the fourth power of temperature. Because the electrochemical performance of SOFC is affected by the temperature, the results of the heat transfer model will also affect the accuracy of the entire electrochemical model. Since the actual interval between the inner surface of the cell and the channel height is much smaller than the length of the cell, the radiation heat transfer between the inner surface of that is approximately the radiation heat transfer between two parallel plates, ignoring the gas radiation. The results in Fig. 4(a) are obtained based on an operating voltage of 0.75V and an emissivity of 0.8. To solve the total, convection, conduction, and radiation heat transfer of all domains inside FC, involving calculation equations including (27), (28) and (29). As shown in Fig. 4(a), the total heat flux is 0.32 W $cm^{-2}$. The parts for the convection, conduction, and radiation account for 75.01 %, 21.86 % and 3.13 %, respectively. It can be seen that the part of radiation heat transfer is apparently less than the heat conductivity. However, the prediction accuracy of the MS-SOFC model can be improved when radiation is modeled. Further in-situ experimental investigation is required to validate the results. It can be observed from Fig. 4(b) that the inclusion of radiation model apparently increases the temperatures along the flow channels. For the anode side, the maximum temperatures with and without radiation are 1010.78 K and 1012.95 K respectively, with corresponding maximum temperature differences of 87.63K and 89.8K, compared to the lowest temperature of the MS-SOFC (the inlet temperatures of anode and cathode are 923.15K); For the

**Table 3**
Main parameters for multi-physical model of the MS-SOFC.

| Property | Value | Unit | Ref. |
|---|---|---|---|
| Ionic conductivity of GDC | $1.1 \times 10^{-1}\exp(3500/T)$ | $S{\cdot}m^{-1}$ | [19] |
| Ionic conductivity of YSZ | $3.34 \times 10^{4}\exp(-10300/T)$ | $S{\cdot}m^{-1}$ | [19] |
| Electrical conductivity of anode reaction layer | $8.0 \times 10^{4}$ | $S{\cdot}m^{-1}$ | [19] |
| Electrical conductivity of cathode reaction layer | $8.4 \times 10^{4}$ | $S{\cdot}m^{-1}$ | [19] |
| Electrical conductivity of cathode diffusion layer | $8.4 \times 10^{4}$ | $S{\cdot}m^{-1}$ | [19] |
| Electrical conductivity of interconnector and metal support | $1.13 \times 10^{6}$ | $S{\cdot}m^{-1}$ | [19] |
| Porosity of the metal support | 0.5 | | |

**Table 4**
Boundary conditions of multi-physical field model for the MS-SOFC.

| Boundary | Variable | Value (unit) |
|---|---|---|
| Terminal anode collector | Electric ground | 0 (V) |
| Terminal cathode collector | Potential | 0.3–1.15 (V) |
| Fuel inlet | Velocity | 0.89 (m $s^{-1}$) |
| | Molar fraction | 0.97:0.03 ($H_2$: $H_2O$) |
| | Temperature | 923.15 (K) |
| Air inlet | Velocity | 3.44 (m $s^{-1}$) |
| | Molar fraction | 0.79:0.21 ($N_2$:$O_2$) |
| | Temperature | 923.15 (K) |

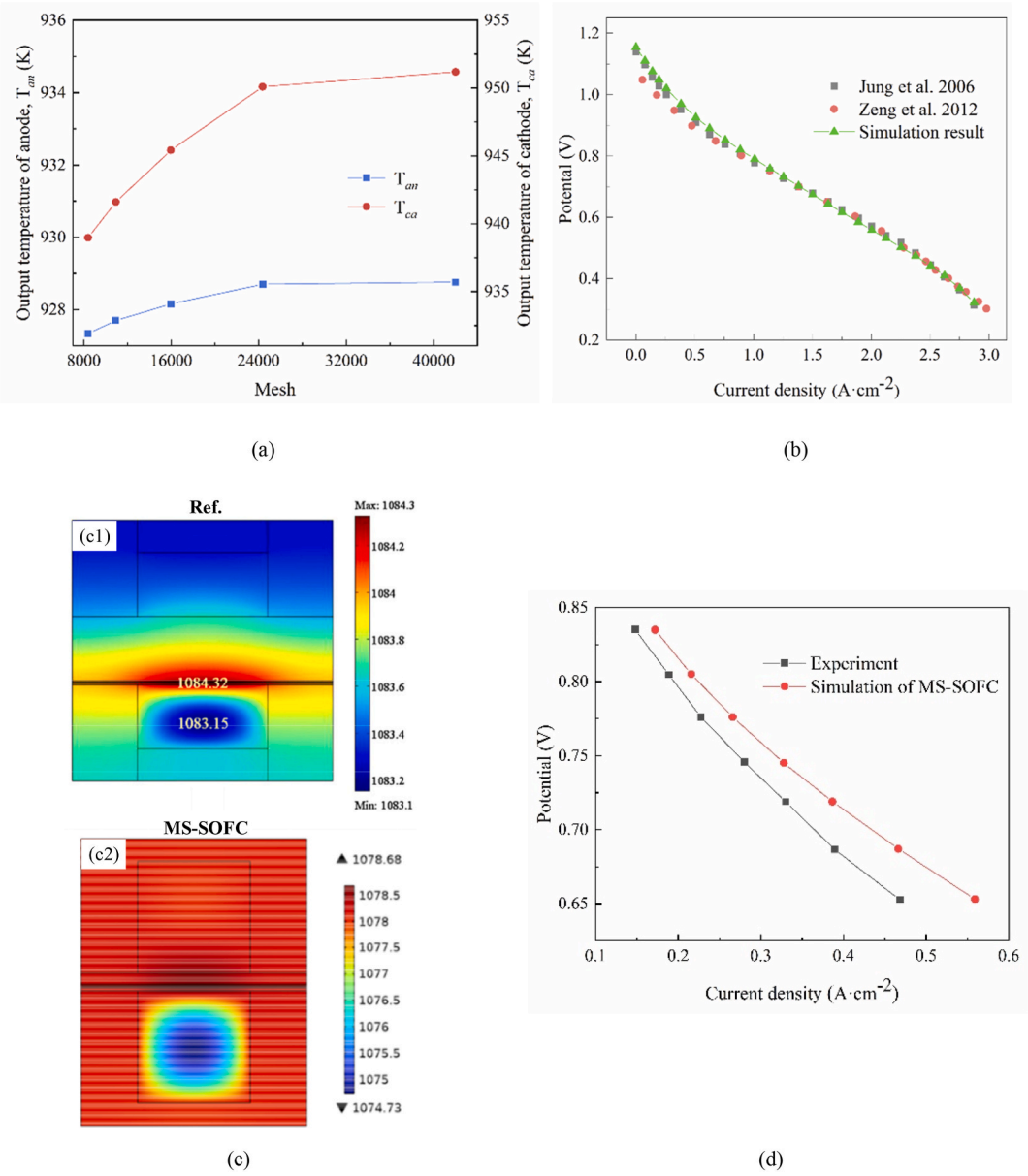


**Fig. 3.** Results for model validation: (a) the grid independence test; (b) validation of radiation heat transfer model with the literature [19,48]; (c) comparison of the temperature fields of the MS-SOFC with the results of the AS-SOFC [19]; (d) comparison of polarization curve of the MS-SOFC with the results of Ceres Power Ltd [28]. [Reproduced with permission. Copyright 2005, 2006, 2012, Elsevier.].

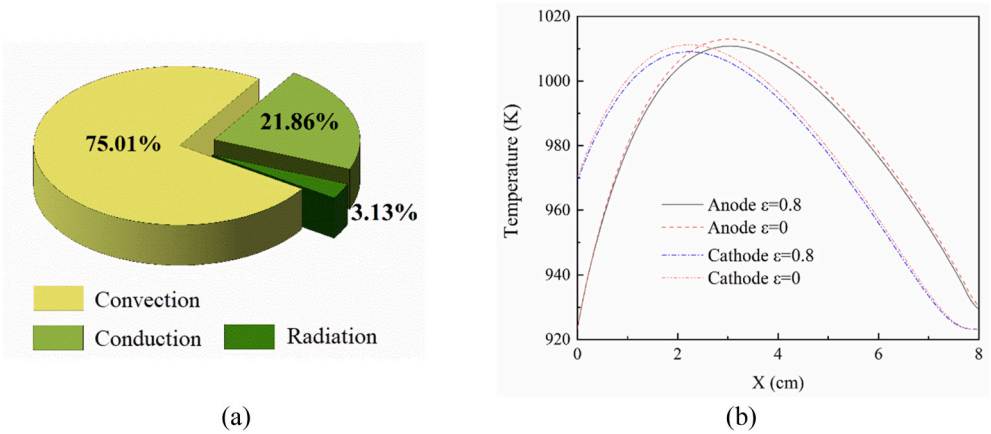


**Fig. 4.** Effects of radiation on the heat transfer in MS-SOFC: (a) heat flux comparison of convection, conduction, and radiation in MS-SOFC; (b) temperature profiles in the flow channels with and without radiation.

cathode side, the maximum temperatures with and without radiation are 1009.07 K and 1011.20 K respectively, with corresponding maximum temperature differences of 85.92K and 88.05K, compared to the lowest temperature of the MS-SOFC (the inlet temperatures of anode and cathode are 923.15K). Compared to no radiation, the maximum temperature difference is reduced by 2.42 % when radiation is taken into account.

$$q_{convection} = \rho C_p \boldsymbol{u} \cdot \nabla T \tag{28}$$

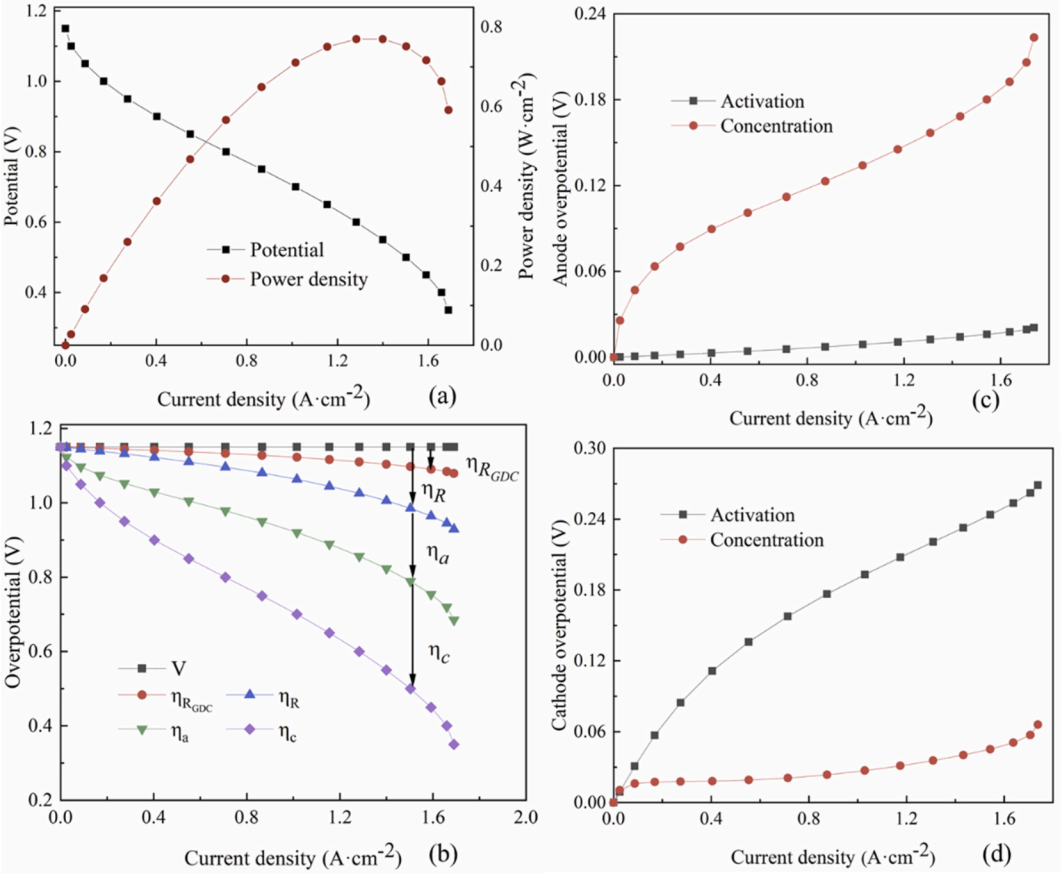


**Fig. 5.** Performance of MS-SOFC under 650 °C: (a) polarization curve; (b) activation and ohmic losses vs. current density; (c) overpotentials of activation and concentration in the anode; (d) overpotentials of activation and concentration in the cathode.

$$q_{conduction} = \kappa \nabla T \tag{29}$$

### 3.2. Polarization curve

Fig. 5(a) shows the estimated polarization curve of the MS-SOFC. With the increase of current density, the operating voltage of the MS-SOFC decreases gradually. When the operating voltage is 0.75 V, the current density is 0.87 A $cm^{-2}$ and the peak power density is 0.65 W $cm^{-2}$. Fig. 5(b) delineates the variations of polarization losses as a function of current density. The ohmic loss is a linear function of the current density when the operating temperature is fixed. As shown in Fig. 5(b), the ohmic loss of the GDC electrolyte $\eta_{R_{GDC}}$ accounts for only 32.04 % of the overall ohmic loss $\eta_R$, exhibiting GDC has a superior advantage in the MS-SOFC operating under the intermediate temperature. The overpotential in the anode incorporates the anodic activation overpotential due to resistance to charge exchange reactions, the ohmic overpotential due to resistance to electron and ion transports in the anode reaction layer and the electron flow in the metal support, and the anodic concentration overpotential due to resistance to the flow of reactants through the porous anode. Cathode overpotential also includes similar terms. It can be seen from Fig. 5(c) that the activation overpotential of the anode maintains at a small order of magnitude and the concentration overpotential gradually increases with the increase of current

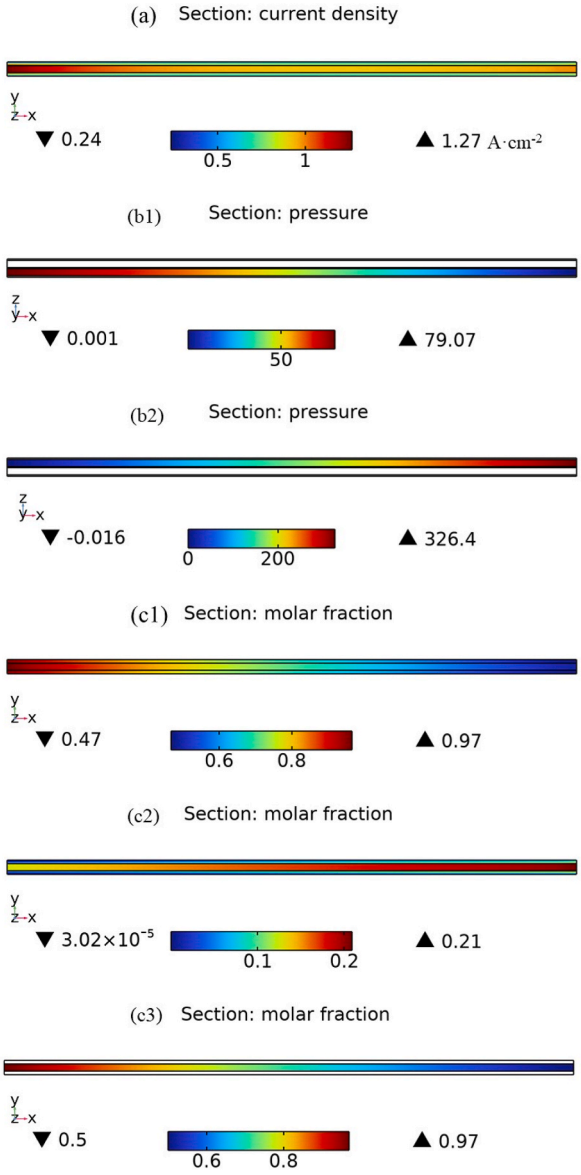


**Fig. 6.** Physical fields distributions in the MS-SOFC along the flow direction: (a) current density on XY section; (b) pressure on XZ section at Y = 0.1 cm; (c) molar fraction on XY section.

density. Compared with the anode side, the overpotentials of activation and concentration manifest opposite trends on the cathode side, as depicted in Fig. 5(d). When the current density is 0.09 A $cm^{-2}$, the concentration overpotential of the anode and cathode is 0.05 V and 0.02 V, respectively. However, when the current density is increased to 1.69 A $cm^{-2}$, the concentration overpotential is 0.22 V and 0.07 V, respectively. A relatively large concentration overpotential in the anode is mainly because the reactants need to overcome the resistance of the metal support to reach the three-phase reaction interfaces, which indicates that the structure of the metal support has a serious impact on the diffusion of gas components, and then affects the performance of the MS-SOFC. It is worth noting that when the current density is 0.09 A $cm^{-2}$, the activation overpotentials in Fig. 5(c) and (d) are 0.588 mV and 30.9 mV, respectively. When the current density is 1.69 A $cm^{-2}$, the associated activation overpotentials are 20.7 mV and 269 mV, respectively. Compared to the anode, the activation overpotential of the cathode is approximately two orders of magnitude larger, indicating that

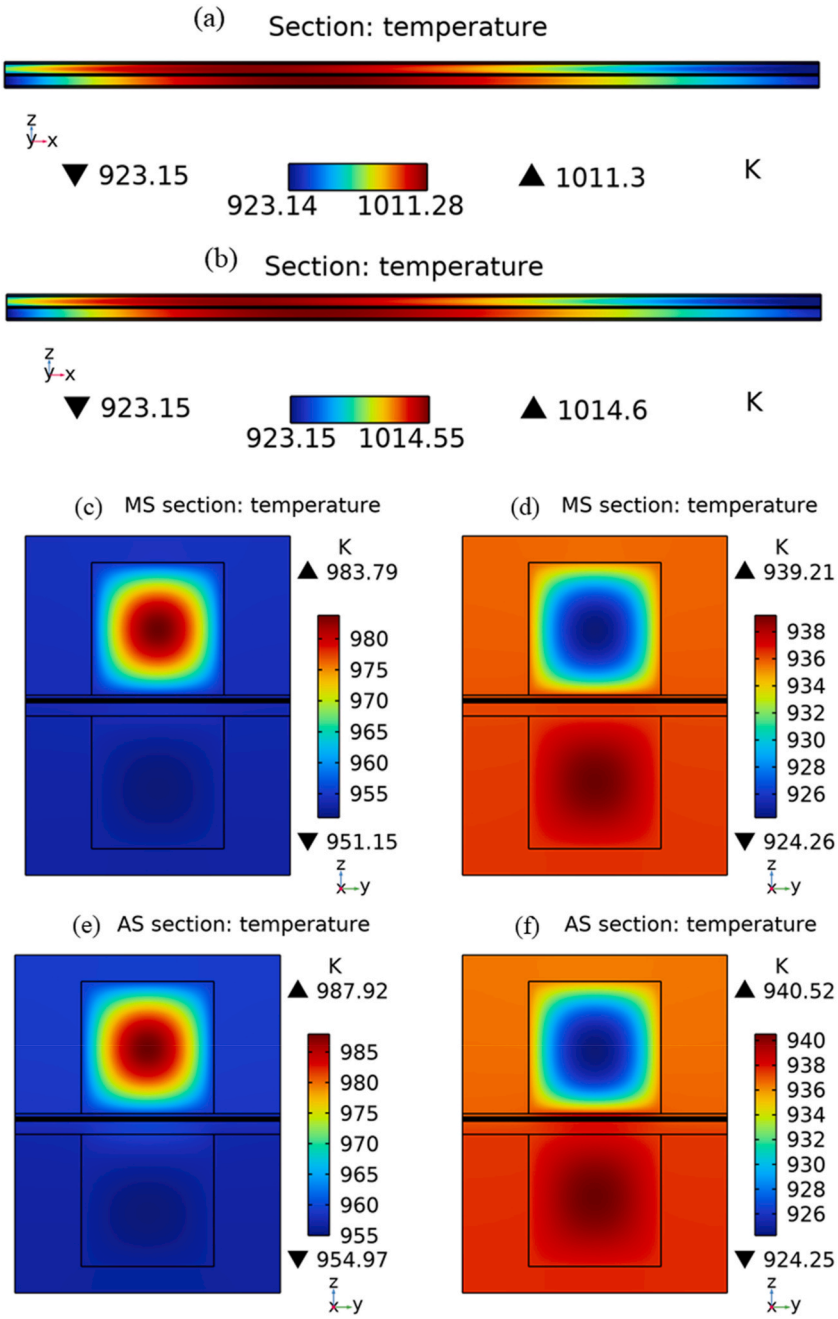


**Fig. 7.** Temperature distributions in the MS-SOFC and AS-SOFC on two typical YZ sections: (a) and (b) temperature on XZ section at Y = 0.1 cm, (a) temperature of MS-SOFC, (b) temperature of AS-SOFC; (c) and (e) X = 0.4 cm; (d) and (f) X = 7.6 cm, (c) and (d) temperature of MS-SOFC, (e) and (f) temperature of AS-SOFC.

the oxygen reduction reaction of the cathode is more difficult to occur.

### 3.3. Distributions of physical fields in MS-SOFC

The distributions of physical fields for the MS-SOFC are analyzed in this section and the results are shown in Fig. 6. Fig. 6(a) displays the distribution of current density in electrolyte. The zone with a high current density is concentrated near the inlet of the anode, gradually decreasing along the direction from the inlet to the outlet. The current density at the entrance is 1.27 A $cm^{-2}$, while it is 0.24 A $cm^{-2}$ at the exit. The magnitude of change in current density is 1.03 A $cm^{-2}$. Fig. 6(b1) and (b2) illustrate the pressure drops inside the flow channels of the anode and cathode, respectively. The maximum pressure drops in the anode and cathode are 79.07 Pa and 326.4 Pa, respectively, which is below the limit value. Fig. 6(c1) represents the distributions of the molar fraction of the hydrogen in the anode electrode and metal support of the MS-SOFC. Hydrogen has a fuel utilization of 83 %. The concentration of hydrogen decreases significantly along the flow direction in the anode, resulting in a large difference of concentrations between the inlet and outlet. As a result, the current density near the inlet of hydrogen increases while the current density near the outlet decreases. The variation trend of current density is similar to that of the hydrogen partial pressure. Additionally, the relatively low current density occurs in the zone where the ribs and the electrodes contact. Fig. 6(c2) delineates the distributions of the molar fraction of the oxygen in the cathode reaction layer and diffusion layer of the MS-SOFC. It shows that the variation of oxygen is small, because excess air is usually passed through the cathode flow channel. Furthermore, the molar fractions of $H_2$ in the anode and the flow passages are compared in Fig. 6(c1) and (c3). The molar fraction of $H_2$ inside the passage is relatively higher at the same position. The average $H_2$ molar fraction in the anode electrode and the metal support are 0.47 and 0.5 at the outlet, respectively, mainly due to the transfer of specie to the porous electrode. There will be an apparent change in gas concentration due to diffusion resistance in the electrode and the metal support. Therefore, it is necessary to reasonably design the structure of the metal support to avoid serious impact on gas diffusion. How and to what extent the metal support affects the electrical performance and temperature of the MS-SOFC will be described in detail in the next section.

Compared with the AS-SOFC operating at 750 °C, the working temperature of the MS-SOFC has decreased to an intermediate temperature of 650 °C owing to the employment of GDC electrolyte instead of YSZ in the AS-SOFC. However, such a high temperature atmosphere still poses a great challenge, because the high temperature and the temperature variation will have a negative effect on the mechanical properties of the cell, resulting in thermal fatigue, delamination, and even fracture of the cell. In addition, temperature changes will also affect the electrical performance, such as the distributions of the potential, current density, and electrical power. Therefore, the management and control of the cell temperature is particularly important. Besides, the gas flow in the anode has an effect on the thermal-electric performance of the FC itself. Moreover, the metal support of MS-SOFC is relatively thick, and the thermal conductivity is large, hence the temperature of the MS-SOFC is affected greatly, which needs to be taken into account. In order to further quantify the influence of metal support on the internal temperature of MS-SOFC, the temperature distribution of the AS-SOFC was calculated under the same operating conditions as listed in Table 4. Moreover, a comparison with the AS-SOFC is conducted. In order to ensure the principle of single variable, the structure and the materials of this AS-SOFC is consistent with that of the MS-SOFC introduced in Section 2 with the metal support is replaced with an anode support. The gas flow of the AS-SOFC is also counter-flow arrangement. Fig. 7 further explores the influence of the metal support on the temperature distribution in the MS-SOFC. In this figure, the results of the AS-SOFC are obtained under the same conditions. The temperature fields on the anode side including the electrolyte, the anode reaction layer, the metal or anode support layer, the anode flow channel, and the interconnect are compared. Fig. 7(a) and (b) give the temperature distributions at the central position where the electrochemical reaction is the most intense. The temperature of the MS-SOFC increases first and then gradually decreases from the inlet to the outlet along the X direction owing to the mutual interaction of heat transfer and electrochemical reactions. The maximum temperature for the MS-SOFC is 1011.3 K with a temperature difference of 88.15 K, while the peak temperature is 1014.6 K for the AS-SOFC with a temperature difference of 91.45 K. Compared to the AS-SOFC with a similar structure of the MS-SOFC, the temperature difference amplitude of the MS-SOFC has been reduced by 3.61 %.

The temperature variation inside an SOFC during operation can affect the thermal stress of ceramic materials. Excessive thermal stress will damage the bonding between the ceramic layer and the metal support, seriously affecting the performance and lifespan of the cell. A further analysis of temperature distribution at different locations inside the entire MS-SOFC provides a reference for optimizing heat transfer within the cell. Fig. 7(c), (d), (e), and (f) display the magnified views of two typical sections at X = 0.4 cm and X = 7.6 cm away from the inlet of the anode flow passage. The internal temperature distribution of the MS-SOFC is similar with that of the AS-SOFC. In Fig. 7(c), the maximum temperature is located at the center of the flow passage of the cathode, approximately 983.79 K, decreasing gradually towards the surrounding to 954.2 K. Meanwhile, the minimum temperature occurs at the center of the flow passage of the anode, approximately 951.15 K, and increases outwards gradually to 952.91K. Because the oxidation reactions in the MS-SOFC are exothermic, the temperature of the positive electrode-electrolyte-negative electrode (PEN) layer is relatively high. The average temperature of the main GDC electrolyte is 954.32 K and gradually diminishes along the X-axis in both directions. The average temperature is 954.19 K for the anode reaction layer and 954 K for the metal support. The maximum temperature difference across the entire section is 32.64 K. In comparison, the maximum temperature in Fig. 7(d) appears at the center of the flow passage of the anode, approximately 939.21 K, and decreases outwards to 936.35 K. Accordingly, the minimum temperature is located at the center of the flow passage of the cathode, approximately 924.26 K, gradually increasing outwards to 935.87 K. The average temperature of the main GDC electrolyte is 936.45 K, which decreases slightly along the X-axis in both directions. The average temperature is 936.44 K for the anode reaction layer and 936.41 K for the metal support. The maximum temperature difference across the entire section decreases to 14.95 K. In Fig. 7(e) and (f), at X = 0.4 cm, the maximum and minimum temperatures of the AS-SOFC are 987.92 K and 954.97 K,

respectively, and the temperature difference is 32.95 K. At X = 7.6 cm, the maximum and minimum temperatures of the AS-SOFC are 940.52 K and 924.25 K, respectively, and the temperature difference is 16.27 K. Compared to the AS-SOFC, the temperature difference of the MS-SOFC decreases by 0.94 % and 8.11 %, respectively. From Table 2, the thermal conductivity of the metal support layer is 20 W $m^{-1}$ $K^{-1}$, while the thermal conductivity of the anode Ni/GDC is only 6.0 W $m^{-1}$ $K^{-1}$. Compared with the anodic material, the thermal conductivity of the metal support is 3.33 times greater. Therefore, it is evident that the use of metal support is more conducive to the conduction of ohmic heat inside the electrolyte, which is beneficial for improving the uniformity of internal temperature field, reducing thermal stress, and increasing the life and reliability of the MS-SOFC.

### *3.4. Effect of metal support structure*

The selection of metal support structure parameters in this section is based on the parameter range for optimal design of metal support structure as described in the patent of Ceres Power [51]. The initial temperature, pressure, and voltage are set to 923.15 K, 0.1 MPa, and 0.75V, respectively. Fig. 8 shows the effect of the structure of metal support on the thermal-electric performance of MS-SOFC, where Fig. 8(a) shows the effect of the porosity of the metal support where the operating conditions are the same as Table 2. Fig. 8(b) shows the influence of the thickness of the metal support. It can be seen that the current density and temperature distribution of MS-SOFC exhibit opposite trends with regard to the porosity and the thickness although the magnitude is small. As can be seen from Fig. 8(a), when the support thickness is 100 μm and the porosity increases from 0.45, 0.50, 0.55, 0.60 and 0.65, the current density is 8653.13 A $m^{-2}$,8653.25 A $m^{-2}$,8652.71 A $m^{-2}$,8651.88 A $m^{-2}$ and 8650.51 A $m^{-2}$, respectively. The current density gradually increased and then gradually decreases. When the porosity is 0.50, the peak value of current density appears. The temperature increases gradually and slowly at 982.07K, 982.24K, 982.42K, 982.61K and 982.81K, respectively. As can be seen from Fig. 8(b), when the porosity is 0.50 and the support thickness increases from 50 μm, 100 μm, 150 μm, 200 μm and 250 μm,the current density is 8638.36 A $m^{-2}$, 8653.21 A $m^{-2}$, 8661.22 A $m^{-2}$, 8668.57 A $m^{-2}$ and 8675.26 A $m^{-2}$, respectively, and the current density gradually increased slowly. Its temperature is 982.79K, 982.24K, 981.86K, 981.47K and 981.09K, respectively, and the temperature gradually decrease.

The porosity and thickness of the metal support have different effects on the thermo-electric performance of the FC, mainly because of their various mechanisms. In terms of porosity, it not only affects the mass transport, but also affects the charge collection between the support and the interconnect. Therefore, the influence of the metal support on the performance of the FC is the results of the trade-off of these two factors. For the thickness, the thicker the support is, the more difficult the diffusion of the reaction gas in the beginning part of the flow channel, enhancing the concentrations of the reactant gases at the downstream. On the other hand, the temperature in the middle zone is the highest along the flow direction. As the thickness of the metal support increases, a more uniform temperature distribution is obtained due to a better thermal conductivity of the metal support and the temperature at the region in the proximity of the outlet is improved. As a result, the current density in the beginning part of the flow channel decreases whereas the current densities in the middle zone and the downstream part increase, leading to a slightly improvement of the overall current density in the considered range of the metal support thickness. In addition, due to the electrochemical reaction in the FC, the internal electric field changes, which affects the internal temperature distribution. As the increase of the porosity, due to the decrease of the concentration polarization, the heat generated in the anode due to the exothermic electrochemical reaction increases. However, the heat capacity of the metal support declines. Therefore, influenced by these two factors, the temperature increases slightly. When the thickness of the metal support enlarges, the heat capacity of the metal support increases. Meanwhile, more reaction gases inside the metal support which of temperature is lower, the lower the temperature will be correspondingly because of the gas heat transfer. In general, the influence of the structure parameters of the metal support on the performance evaluation of FC is complicated, and the structure of the metal support needs to be carefully designed.

## 4. Conclusion

A 3D multi-physical model was designed for an MS-SOFC and the internal thermohydraulic and electrochemical performances were investigated. First, the overall polar curve of the MS-SOFC was obtained according to the simulation results. Then, the distributions of velocity and species concentration were analyzed. The variations of the ionic and electronic current densities were explored as well. Finally, the temperature distributions inside the MS-SOFC were discussed. The main conclusions are summarized as follows.

(1) With the thermal radiation model using a discrete method, the prediction of temperature field of the MS-SOFC is improved. The convection heat flux, conduction heat flux and radiation heat flux account for 75.01 %, 21.86 % and 3.13 % of the total heat flux, respectively. With and without radiation, the corresponding maximum temperature differences in the anode channel are 87.6 K and 89.8 K; the maximum temperature differences in the cathode channel are 85.9 K and 88.1 K. Compared to that without radiation, the maximum temperature difference is reduced by 2.42 % when there is radiation.

(2) Anode concentration overpotential is mainly due to the reactants need to overcome the resistance of the metal support to reach the three-phase reaction interfaces, which indicates that the structure of the metal support has a serious impact on the diffusion of gas components, and then affects the performance of the MS-SOFC. When the current density is 0.09 A $cm^{-2}$, the concentration overpotential of anode and cathode is 0.05 V and 0.02 V, respectively. However, when the current density is increased by 1.69 A $cm^{-2}$, the concentration overpotential is 0.22 V and 0.07 V, respectively.

(3) Using the metal support is beneficial for improving the temperature uniformity inside the SOFC. The maximum temperature for the MS-SOFC is 1011.3 K with a temperature difference of 88.2 K, while that for the AS-SOFC is 1014.6 K with a temperature

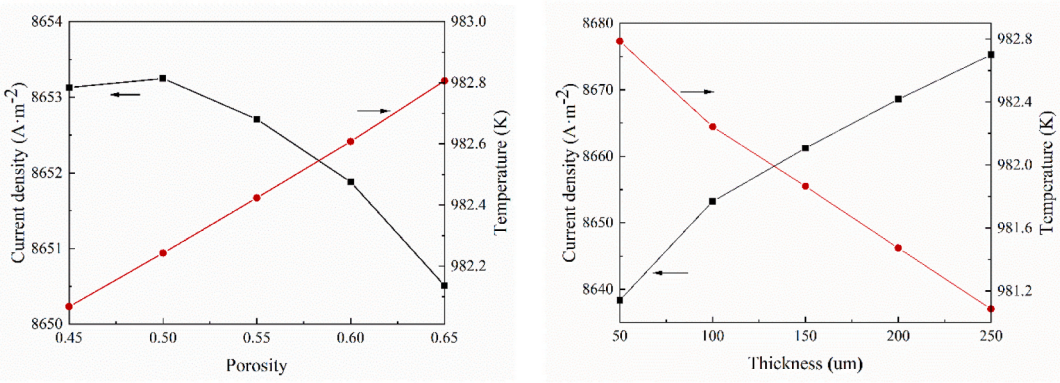


**Fig. 8.** Effect of metal support on thermal-electrical performance the MS-SOFC: (a) the porosity; (b) the thickness.

difference of 91.5 K. Compared to the AS-SOFC, the temperature difference amplitude of the MS-SOFC has been reduced by 3.61 %. Compared to the AS-SOFC, the temperature difference of MS-SOFC decreases by 0.94 % at X = 0.4 cm and 8.11 % at X = 7.6 cm, respectively. Therefore, the metal support is conducive to improving the conduction of ohmic heat inside the electrolyte layer and the temperature uniformity, which is important for the reduction of internal thermal stress, and enhancement of the life and reliability.

## Funding

This research work was supported by the National Key Research and Development Program of China (Grant No. 2021YFB2500400).

## Data and code availability statement

Data will be made available on request.

## CRediT authorship contribution statement

**Mengru Zhang:** Writing – original draft, Visualization, Software, Methodology, Investigation, Formal analysis, Data curation. **Enhua Wang:** Writing – review & editing, Validation, Formal analysis, Conceptualization. **Meng Ni:** Writing – review & editing, Validation, Formal analysis, Conceptualization. **Keqing Zheng:** Writing – review & editing, Validation, Investigation, Formal analysis, Conceptualization. **Minggao Ouyang:** Supervision, Resources. **Haoran Hu:** Project administration, Funding acquisition, Conceptualization. **Hewu Wang:** Validation, Project administration. **Languang Lu:** Visualization, Resources. **Dongsheng Ren:** Resources, Data curation. **Youpeng Chen:** Resources, Methodology, Data curation.

## Declaration of competing interest

The authors declare that they have no known competing financial interests or personal relationships that could have appeared to influence the work reported in this paper.

## References

[1] M. Zhang, L. An, E. Wang, et al., Effects of sintering parameters on the low-temperature densification of GDC electrolyte based on an orthogonal experiment, J. Catal. 12 (8) (2022) 831.
[2] Q. Yang, M. Chen, B.S. Teketel, D. Tian, et al., Influences of equal A-site rare-deficiency or B-site high-valent metal doping on NdBaFe2O5+ δ employed as the symmetrical electrode for solid oxide fuel cells, J. Journal of Alloys and Compounds 918 (2022) 165368.
[3] K. Lee, S. Kang, K. Ahn, Development of a highly efficient solid oxide fuel cell system, J. Applied Energy 205 (2017) 822–833.
[4] A. Shi, Y. Kong, Z. Li, et al., Performance analysis of series connected cathode supported tubular SOFCs, Int. J. Electrochem. Sci. 18 (5) (2023) 100126.
[5] P. Blennow, J. Hjelm, T. Klemenso, et al., Development of planar metal supported SOFC with novel cermet anode, J. ECS Transactions 25 (2) (2009) 701–710.
[6] R. Zhan, Y. Wang, M. Ni, et al., Three-dimensional simulation of solid oxide fuel cell with metal foam as cathode flow distributor, J. International Journal of Hydrogen Energy 45 (11) (2020) 6897–6911.
[7] M.C. Tucker, Progress in metal-supported solid oxide fuel cells: a review, J. Journal of Power Sources 195 (15) (2010) 4570–4582.
[8] N.Q. Minh, T. Takahashi, Science and Technology of Ceramic Fuel Cells. Science and Technology of Ceramic Fuel Cells, Elsevier, 1995.
[9] H. Chang, J. Yan, H. Chen, G. Yang, et al., Preparation of thin electrolyte film via dry pressing/heating/quenching/calcining for electrolyte-supported SOFCs, J. Ceramics International 45 (8) (2019) 9866–9870.

[10] G. Chen, G. Guan, Y. Kasai, et al., Nickel volatilization phenomenon on the Ni-CGO anode in a cathode-supported SOFC operated at low concentrations of $H_2$, J. International journal of hydrogen energy 37 (1) (2012) 477–483.
[11] H.J. Cho, K.J. Kim, Y.M. Park, et al., Flexible solid oxide fuel cells supported on thin and porous metal, international journal of hydrogen energy, J. International journal of hydrogen energy 41 (22) (2016) 9577–9584.
[12] T. Shimura, T. Nagasawa, N. Shikazono, et al., Three-dimensional numerical simulation of oxygen isotope transport in lanthanum strontium manganese-Yttria-stabilized zirconia cathode of solid oxide fuel cell, J. International Journal of Hydrogen Energy 48 (50) (2023) 19233–19247.
[13] K.K. Śreniawski, M. Chalusiak, M. Moździerz, et al., Transport phenomena in a banded solid oxide fuel cell stack—Part 1: model and validation, transport phenomena in a banded solid oxide fuel cell stack—Part 1: model and validation.", Energies 16 (11) (2023) 4511.
[14] S. Youcef, Z. Bariza, M. Houcine, et al., Three-dimensional numerical study of the anode supported intermediate temperature solid oxide fuel cell overheating, J. International journal of Heat and Technology 37 (4) (2019) 1099–1106.
[15] L. Yang, W. He, J. Wang, et al., An accurate and efficient multiphysics 3D model for the design and operation analysis of production-scale solid oxide cell stacks, J. International Journal of Hydrogen Energy 50 (2024) 1075–1086.
[16] J. Liao, H. Jie, Q. Hu, et al., Understanding performance difference in the scale-up of flat-chip solid oxide fuel cell: an experimental and numerical study, J, Sustain. Energy Technol. Assessments 63 (2024) 103649.
[17] Q. Shen, S. Li, G. Yang, et al., Analysis of heat and mass transport characteristics in anode-supported solid oxide fuel cells at various operating conditions, J. Numerical Heat Transfer, Part A: Applications 75 (8) (2019) 509–522.
[18] N. Russner, S. Dierickx, A. Weber, et al., Multiphysical modelling of planar solid oxide fuel cell stack layers, J. Journal of power sources 451 (2020) 227552.
[19] M. Zeng, J. Yuan, J. Zhang, et al., Investigation of thermal radiation effects on solid oxide fuel cell performance by a comprehensive model, J. Journal of Power Sources 206 (2012) 185–196.
[20] W.C. Tan, H. Iwai, M. Kishimoto, et al., Quasi-three-dimensional numerical simulation of a solid oxide fuel cell short stack: effects of flow configurations including air-flow alternation, J. Journal of Power Sources 400 (2018) 135–146.
[21] D. Chen, Y. Zhu, S. Han, et al., Investigate the effect of a parallel-cylindrical flow field on the solid oxide fuel cell stack performance by 3D multiphysics simulating, J. Journal of Energy Storage 60 (2023) 106587.
[22] Y. Liu, Y. Xu, Y. Ya, et al., Effects of bipolar plate flow channel configuration on thermal-electric performance of direct ammonia solid oxide fuel cell: Part II-Promoting in-cell ammonia endothermic decomposition via a novel parallel S-type channel arrangement, J. International Journal of Hydrogen Energy 55 (2024) 1217–1233.
[23] M. Guo, Q. He, C. Cheng, et al., New interconnector designs for electrical performance enhancement of solid oxide fuel cells: a 3D modelling study, J. Journal of Power Sources 533 (2022) 231373.
[24] M. Ilbas, B. Kumuk, Numerical modelling of a cathode-supported solid oxide fuel cell (SOFC) in comparison with an electrolyte-supported model, J. Energy Inst. 92 (3) (2019) 682–692.
[25] D. Udomsilp, J. Rechberger, R. Neubauer, et al., Metal-supported solid oxide fuel cells with exceptionally high power density for range extender systems, Cell Reports Physical Science 1 (6) (2020).
[26] Q. Li, X. Wang, L. Jia, et al., High performance and carbon-deposition resistance metal-supported solid oxide fuel cell with a nickel–manganese spinel modified anode, J. Materials Today Energy 17 (2020) 100473.
[27] C. Adjiman, A. Atkinson, A. Azad, et al., A review of progress in the UK supergen fuel cell programme, J. ECS Transactions 25 (2) (2009) 35–42.
[28] R.T. Leah, N.P. Brandon, P. Aguiar, Modelling of cells, stacks and systems based around metal-supported planar IT-SOFC cells with CGO electrolytes operating at 500–600° C, J. Journal of Power Sources 145 (2) (2005) 336–352.
[29] M. Zhang, E. Wang, J. Mao, Performance analysis of a metal-supported intermediate-temperature solid oxide electrolysis cell, J. Frontiers in Energy Research 10 (2022) 888787.
[30] J. Park, Y.M. Kim, J. Bae, A numerical study on the heat and mass transfer characteristics of metal-supported solid oxide fuel cells, J. International journal of hydrogen energy 36 (4) (2011) 3167–3178.
[31] G. Brus, J.S. Szmyd, Numerical modelling of radiative heat transfer in an internal indirect reforming-type SOFC, J. Journal of Power Sources 181 (1) (2008) 8–16.
[32] A. Bone, Leah R. Adam, et al., Electrolyte Forming Process, 2020. P.CA2974772C.
[33] Y.J. Kim, M.C. Lee, Numerical investigation of flow/heat transfer and structural stress in a planar solid oxide fuel cell, J. International Journal of Hydrogen Energy 42 (29) (2017) 18504–18513.
[34] Kim YJ, Lee MC. The influence of flow direction variation on the performance of a single cell for an anode-substrate flat-panel solid oxide fuel cell, J. International journal of hydrogen energy 45(39), 20369-20381. .
[35] X. Li, W. Shi, M. Han, Optimization of interconnect flow channels width in a planar solid oxide fuel cell, J. International Journal of Hydrogen Energy 43 (46) (2018) 21524–21534.
[36] Q. Chen, M. Zeng, J. Zhang, et al., Optimal design of bi-layer interconnector for SOFC based on CFD-Taguchi method, J. International Journal of Hydrogen Energy 35 (9) (2010) 4292–4300.
[37] Q. Chen, Q. Wang, J. Zhang, et al., Effect of bi-layer interconnector design on mass transfer performance in porous anode of solid oxide fuel cells, J, Int. J. Heat Mass Tran. 54 (9–10) (2011) 1994–2003.
[38] X. Zhang, L. Wang, M. Espinoza, et al., Numerical simulation of solid oxide fuel cells comparing different electrochemical kinetics, J. International Journal of Energy Research 45 (9) (2021) 12980–12995.
[39] R. Bove, S. Ubertini, Modeling Solid Oxide Fuel Cells: Methods, Procedures and Techniques, M, Springer Science & Business Media, 2008.
[40] P. Iora, P. Aguiar, C.S. Adjiman, et al., Comparison of two IT DIR-SOFC models: impact of variable thermodynamic, physical, and flow properties. Steady-state and dynamic analysis, J, Chem. Eng. Sci. 60 (11) (2005) 2963–2975.
[41] M.M. Hussain, X. Li, I. Dincer, Mathematical modeling of planar solid oxide fuel cells, J. Journal of Power Sources 161 (2) (2006) 1012–1022.
[42] M.M. Hussain, X. Li, I. Dincer, A general electrolyte–electrode-assembly model for the performance characteristics of planar anode-supported solid oxide fuel cells, J. Journal of Power Sources 189 (2) (2009) 916–928.
[43] J. Yuan, B. Sundén, On continuum models for heat transfer in micro/nano-scale porous structures relevant for fuel cells, J. International Journal of Heat and Mass Transfer 58 (1–2) (2013) 441–456.
[44] G.F. Al-Sumaily, A. Nakayama, J. Sheridan, et al., The effect of porous media particle size on forced convection from a circular cylinder without assuming local thermal equilibrium between phases, J. International Journal of Heat and Mass Transfer 55 (13–14) (2012) 3366–3378.
[45] M. García-Camprubí, H. Jasak, N. Fueyo, CFD analysis of cooling effects in H2-fed solid oxide fuel cells, J. Journal of Power Sources 196 (17) (2011) 7290–7301.
[46] A.C. Yunus, Heat Transfer: a Practical Approach, vol. 210, J. MacGraw Hill, New York, 2003.
[47] C. Bao, N. Cai, E. Croiset, An analytical model of view factors for radiation heat transfer in planar and tubular solid oxide fuel cells, J. Journal of Power Sources 196 (6) (2011) 3223–3232.
[48] H.Y. Jung, W.S. Kim, S.H. Choi, et al., Effect of cathode current-collecting layer on unit-cell performance of anode-supported solid oxide fuel cells, J. Journal of Power Sources 155 (2) (2006) 145–151.
[49] M. Guo, G. Xiao, J. Wang, et al., Parametric study of kW-class solid oxide fuel cell stacks fueled by hydrogen and methane with fully multiphysical coupling model, J. International Journal of Hydrogen Energy 46 (14) (2021) 9488–9502.
[50] A.N. Celik, Three-dimensional multiphysics model of a planar solid oxide fuel cell using computational fluid dynamics approach, J. International Journal of Hydrogen Energy 43 (42) (2018) 19730–19748.
[51] H.C.B. Steele, A. Atkinson, A.J. Kilner, Fuel Cell. (2004). GB2368450(B).